Volume 13 | Number 3 | 3 February 2026

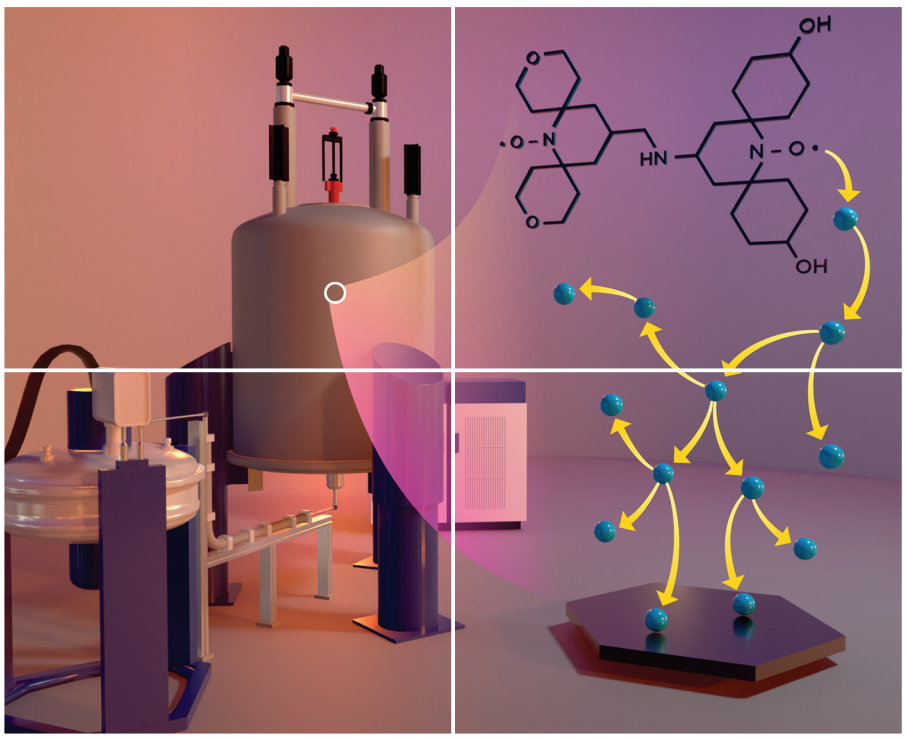

INORGANIC CHEMISTRY

FRONTIERS

CCS 中国化学会 CHINESE CHEMICAL SOCIETY
PEKING UNIVERSITY 1898
ROYAL SOCIETY OF CHEMISTRY
rsc.li/frontiers-inorganic

INORGANIC CHEMISTRY
FRONTIERS

RESEARCH ARTICLE

View Article Online
View Journal | View Issue

Cite this: *Inorg. Chem. Front.*, 2026, **13**, 950

Localizing tetrahedral aluminum in nitrate-bearing gibbsite to constrain defect-impurity coupling

Trent R. Graham, *[a] Micah P. Prange, [a] Xin Zhang, [a] J. David Bazak, [a] Nancy M. Washton,[a] Khashayar Ghandi, [b] Gregory K. Schenter [a] and Carolyn I. Pearce [a,c]

Received 13th August 2025,
Accepted 25th October 2025

DOI: 10.1039/d5qi01703c

rsc.li/frontiers-inorganic

The enhanced radiolytic stability of gibbsite (α-$Al(OH)_3$) containing trace nitrate (NO_3^-) is a phenomenon in nuclear waste management, but its structural origins remain unresolved. Motivated by the detection of minority tetrahedral aluminum (T_d) defects in synthetic gibbsite, we hypothesized that these sites may participate in NO_3^- retention or mediate H_2 suppression. To evaluate this, we combined orthogonal techniques comprised of spatially selective solid-state ^{27}Al MAS NMR, comparative spectroscopy, and density functional theory (DFT) modeling. Paramagnetic editing and dynamic nuclear polarization (DNP) MAS NMR confirm that T_d defects are confined to the particle interior. DFT calculations reveal no energetic stabilization of NO_3^- near T_d sites. Comparative NMR analysis shows that T_d is also present in chloride-bearing gibbsite, which exhibits high radiolytic hydrogen yields. These three independent disqualifications rule out T_d as a structural contributor to nitrate-mediated suppression and narrow the scope of defect-driven explanations. The findings redirect mechanistic attention away from coordination defects and toward redox-active impurity pathways, providing a refined foundation for understanding radiation tolerance in $Al(OH)_3$.

Introduction

The radiolytic generation of flammable hydrogen (H_2) gas from aluminum hydroxides is a safety and operational concern in nuclear waste management.[1] Gibbsite (α-$Al(OH)_3$) is a major component of legacy waste sludges,[2,3] and exhibits profoundly different behavior depending on trace impurities incorporated during its formation.[4,5] Recent radiolysis experiments have revealed a dramatic, order-of-magnitude difference in H_2 evolution. Gibbsite containing ~0.6 atom chloride (Cl-gibbsite) yields 0.220 $G(H_2)$ molecules per 100 eV, whereas gibbsite with trace ~0.4 atom % nitrate (NO_3-gibbsite) yields only 0.012 $G(H_2)$.[4] This stark contrast in radiolytic stability occurs despite the materials being nearly indistinguishable by bulk characterization methods, pointing to a mechanism operating at the level of atomic-scale defects.[4]

Minor (<1% of ^{27}Al magic angle spinning nuclear magnetic resonance (MAS NMR) signal) populations of tetrahedral aluminum (T_d) have been observed in synthetic gibbsite under specific formation conditions, particularly at lower synthesis temperatures.[6] Motivated by this structural signature, we hypothesized that T_d defects might play a mechanistic role in the anomalous radiolytic suppression observed in nitrate-bearing gibbsite. Specifically, we considered the possibility that T_d formation could reflect or enable structural accommodation of retained NO_3^-, for example *via* local charge compensation or defect–impurity coupling. To evaluate this, we designed a combined experimental-computational strategy to assess the spatial accessibility, energetic relevance, and correlative behavior of T_d in relation to impurity content. Determining whether T_d sites reside at the surface or in the particle interior was therefore the first step toward assessing their potential for chemical interaction with NO_3^-. This hypothesis also intersects with broader questions about local heterogeneity in gibbsite, which is known to host structurally disordered domains including entrained clusters of octahedral Al.[7] While the present study addresses structural explanations directly, it forms part of a larger effort to resolve the mechanisms of radiological suppression of H_2 in NO_3-gibbsite.

To evaluate the spatial accessibility of T_d defects, we applied two complementary solid-state, MAS-NMR spectroscopy techniques with orthogonal surface sensitivity. Paramagnetic spectral editing was implemented using post-synthesis adsorption of trivalent chromium (Cr^{3+}), which quenches signals from surface-accessible sites through rapid transverse (T_2) relaxation.[8] This method has been successfully

[a]*Pacific Northwest National Laboratory, Richland, 99354, USA.*
E-mail: trent.graham@pnnl.gov
[b]*University of Guelph, Guelph, ON N1G 2 W1, Canada*
[c]*Department of Crop and Soil Sciences, Washington State University, Pullman, 99163, USA*

applied to resolve surface from interior sites in materials ranging from inorganic solids[9] to biological macromolecules.[10,11] Our method leverages the strong adsorption of Cr^{3+} ions to render the chemically-defined near-surface region NMR-silent. Recent spectroscopic and microscopic characterization of this system has confirmed that when introduced post-synthesis, Cr^{3+} adsorbs strongly to the gibbsite surface, forming clusters with minimal penetration into the bulk lattice.[12] Dynamic nuclear polarization (DNP), in contrast, selectively enhances surface-localized signals *via* polarization transfer from an exogenous radical under microwave irradiation.[13,14] Together, these methods provide cross-validation of convergent constraints on the location of T_d defects. This spatial constraint, combined with comparative evidence from chloride-bearing samples and direct energetic evaluation *via* DFT, provided a framework to evaluate T_d defect-impurity coupling in gibbsite.

Results and discussion

The gibbsite samples studied here consist of euhedral, hexagonal nanoplatelets (Fig. 1A) with a BET surface area of ~40 m^2 g^{-1}.[7] ^{27}Al MAS NMR spectra acquired a low-intensity resonance at ~65 ppm, consistent with tetrahedral Al (T_d) (Fig. 2, bottom trace). The broad line shape of this signal suggests a potential distribution of disordered local environments.[15] This defect signal contributes to an increasingly complex view of gibbsite's local structure,[16] but its functional relevance remains unresolved. To evaluate whether T_d defects play a mechanistic role or reflect structural coupling to retained NO_3^-, we conducted spatially selective solid-state NMR experiments to determine their accessibility and location within the material.

We first applied a paramagnetic spectral editing approach (Fig. 1B) using Cr^{3+} ions as surface-selective NMR resonance quenchers to evaluate the spatial accessibility of T_d defects. Cr^{3+} adsorbs strongly to the NO_3-gibbsite surface and induces rapid transverse (T_2) relaxation in nearby nuclei, rendering surface and near-surface environments (~5 Å) NMR-silent.[19] Upon treatment with Cr^{3+} at concentrations up to 100 ppm, no attenuation of the T_d resonance was observed relative to the dominant octahedral Al signal (Fig. 2). The persistence of the T_d signal under these conditions indicates that these sites are not surface-accessible and must reside within the interior of the nanoplatelet. This spatial assignment does not in itself preclude interaction with retained NO_3^-, but it establishes that any such coupling would have to occur in the bulk, not at the surface. The T_d resonance corresponds to <1% of the total ^{27}Al signal, yet its persistence after Cr^{3+} editing demonstrates that it is an interior feature not associated with the surface. Although minor in intensity, its reproducibility across samples and insensitivity to surface quenching confirm that this resonance reflects a real structural population rather than a spectral artifact.

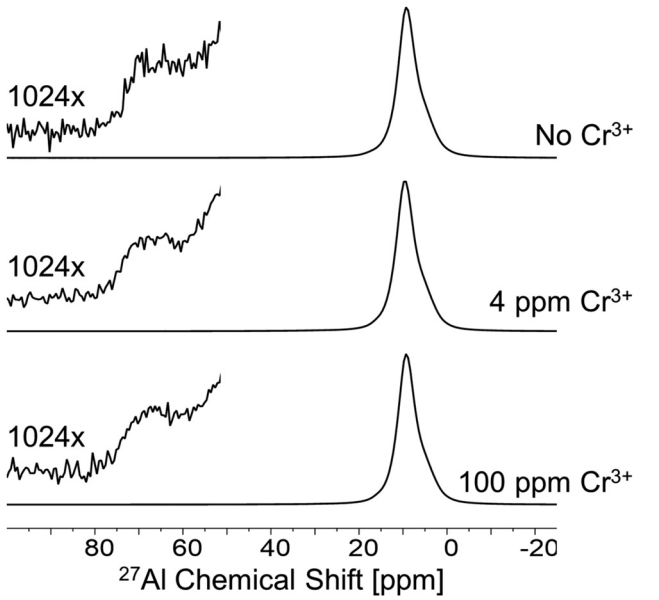

Fig. 2 Paramagnetic editing fails to quench the T_d resonance. ^{27}Al MAS NMR spectra (14.1 T, 20 kHz MAS) of as-synthesized NO_3-gibbsite as well as NO_3-gibbsite following equilibration with 4 and 100 ppm Cr^{3+} solutions. The persistence of the T_d signal relative to the bulk demonstrates its insensitivity to the surface-adsorbed paramagnetic agent.

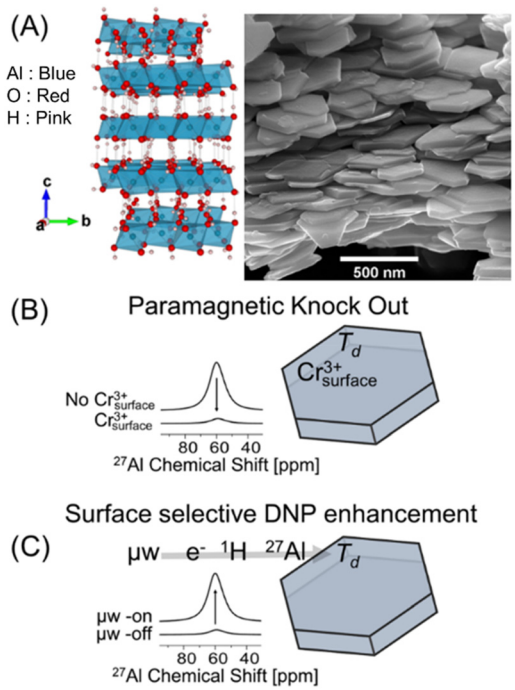

Fig. 1 Experimental strategy for localizing T_d defects in gibbsite. (A) Crystallographic[17] visualization[18] of gibbsite alongside a scanning electron micrograph showing the euhedral, hexagonal nanoplatelet morphology of the synthesized gibbsite. (B) Schematic of the paramagnetic editing experiment, where surface-adsorbed Cr^{3+} renders the near-surface region NMR-silent, leaving subsurface signals unperturbed. (C) Schematic of the DNP-NMR experiment, where an exogenous radical solution selectively enhances NMR signals originating from the particle surface.

Further evidence for the subsurface assignment of T_d defects was acquired with dynamic nuclear polarization (DNP) experiments, which selectively enhance NMR signals originating from surface-accessible sites through microwave-driven polarization transfer from exogenous radicals (Fig. 1C). In NO_3-gibbsite, DNP resulted in enhancement of the surface octahedral Al signal ($\varepsilon \approx 18$), consistent with surface-initiated polarization relay through the hydroxyl network (Fig. 3). However, the T_d resonance showed no preferential enhancement under DNP conditions, indicating that these sites do not reside near the particle surface.

To validate the surface sensitivity of the DNP experiment, we applied the same measurement protocol to a nano-α-Al_2O_3 control material with well-characterized surface chemistry. This system is known to exhibit a high concentration of distinct T_d, pentahedral, and octahedral Al sites located at particle surfaces and grain boundaries.[15] This material showed strong and preferential enhancement of surface-associated resonances, in contrast to the lack of an enhancement for T_d signal in NO_3-gibbsite (Fig. 4). This control supports the interpretation that the lack of enhancement for the T_d signal in gibbsite reflects its spatial isolation, rather than complications in polarization transfer or instrumental sensitivity which are potential confounds given the evolving capabilities of high-field DNP NMR. Taken together with the Cr^{3+} editing data, the DNP results establish that T_d defects in NO_3-gibbsite are structurally real, spatially resolved, and confined to the particle interior.

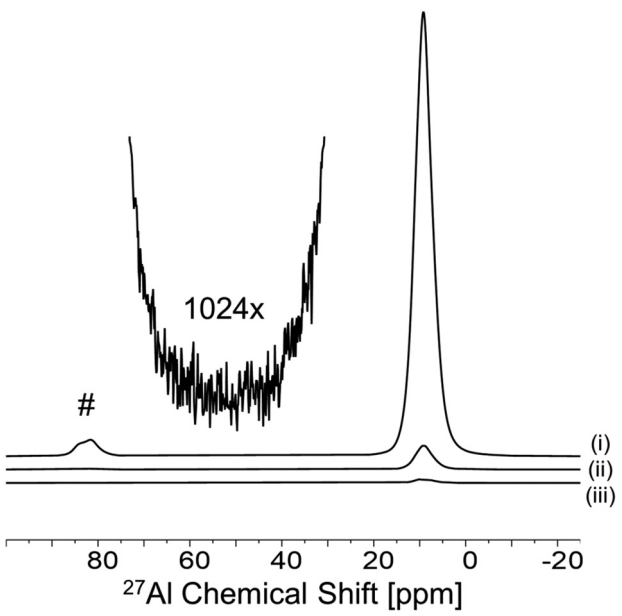

Fig. 3 DNP-NMR fails to preferentially enhance the T_d resonance. ^{27}Al {^1H} cross polarization DNP MAS NMR spectra (18.8 T, 15 kHz MAS, ~100 K) of NO_3-gibbsite. The DNP-off spectrum (middle) is compared to the DNP-on spectrum (top, microwaves on), which shows an enhancement $\varepsilon \approx 18$ of the octahedral Al signal. The T_d resonance at 65 ppm (see inset) shows no such preferential enhancement, indicating its subsurface location. A room-temperature spectrum is provided for comparison (bottom).

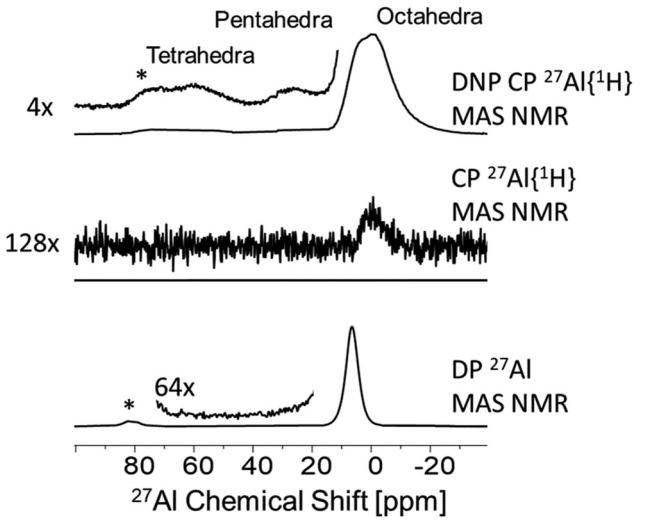

Fig. 4 Validation of the DNP methodology. (A) DNP CP-MAS spectra of a nano-α-Al_2O_3 positive control, demonstrating preferential signal enhancement ($\varepsilon \approx 24$) of known surface Al sites (tetrahedral and pentahedral and perturbed octahedrally coordinated Al), observations that validate the surface-sensitivity of the DNP experiment.

With T_d defects localized to the interior of the NO_3-gibbsite nanoplatelets, we next evaluated whether these sites might structurally interact with NO_3^- impurities. Although NO_3^- is not directly observable in these NMR experiments, its retention following extensive aqueous washing suggests that any incorporated NO_3^- resides within the bulk rather than on the surface. The potential for spatial co-localization between T_d and NO_3^- makes a structural interaction plausible in principle. To assess whether such a coupling is energetically favorable, we performed density functional theory (DFT) simulations to test whether interstitial NO_3^- can induce or stabilize nearby tetrahedral coordination environments in the gibbsite lattice.

Whether interstitial NO_3^- incorporation stabilizes nearby T_d was evaluated using DFT simulations on NO_3^- bearing gibbsite (Fig. 5). Initial configurations were constructed by embedding gas-phase-optimized nitrate–aluminate complexes into

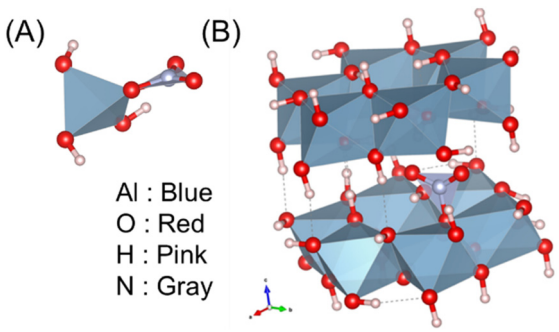

Fig. 5 Evaluation of whether T_d stabilizes NO_3^-. (A) Initial state of nitrate in the gibbsite in which gas phase optimized aluminate tetrahedra nitrate complexes were substituted into the gibbsite lattice. (B) Relaxed structure with nitrate incorporated around Al octahedra.

the gibbsite lattice, followed by structural relaxation under periodic boundary conditions using the RPBE-D3 functional. Across all configurations examined (~10), lattice relaxation did not produce conversion of neighboring octahedral Al into tetrahedral geometry, nor did it yield energetically favored coupling between NO_3^- and existing T_d motifs. Most relaxations resulting in NO_3^- substituting an OH^- group and extending into the interlayer (Fig. 5B). All aluminum centers remained sixfold coordinated following optimization, with some evidence for fivefold coordination. These results are inconsistent with the hypothesis that NO_3^- and T_d form a structurally coupled defect-impurity pair within the bulk lattice. Representative visualizations of attempted nitrate substitutions and a comparison of relative energies are provided in the SI (Fig. S1).

To assess whether the presence of T_d defects correlates with radiolytic suppression, we analyzed ^{27}Al MAS NMR spectra of gibbsite synthesized in the presence of chloride, a system known to produce high radiolytic H_2 yields. These samples exhibited a comparable resonance at ~65 ppm, consistent with T_d, despite their lack of radiolytic stability (Fig. 6). Notably, the figure also shows a ^{27}Al MAS NMR spectra of a second batch of synthesized NO_3-gibbsite. This second batch also displayed the same T_d feature, confirming its reproducibility. Prior reports observed that T_d content decreases as crystallinity improves.[6] To ensure that the observed signal was not an artifact of rotor background or packing, spectra of air-filled rotors were acquired under identical conditions immediately before packing the Cl-gibbsite and second batch of NO_3-gibbsite. The absence of T_d resonances in these controls (Fig. 6) confirmed that the resonance is intrinsic to the samples. This finding demonstrates that the presence of T_d is not unique to nitrate-bearing systems and is not predictive of radiolytic behavior.

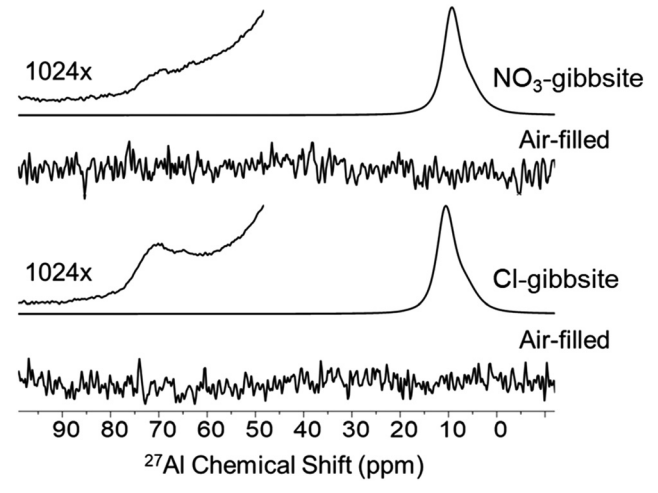

Fig. 6 ^{27}Al MAS NMR spectra at 14.1 T of Cl-gibbsite and a second synthesis batch of NO_3-gibbsite with corresponding air-filled rotors to confirm the absence of spurious T_d signals unrelated to the sample. The number of scans and all other acquisition and post-acquisition processing parameters are identical.

While this result does not exclude the possibility that T_d may participate in other structural processes, it disqualifies the defect as a mechanistic signature of radiolytic suppression in these materials.

Taken together, the results of this study disqualify three structurally plausible but mechanistically unsupported hypotheses linking T_d defects to nitrate-mediated radiolytic suppression of H_2 yield in gibbsite. First, spatially selective NMR techniques establish that T_d defects are sequestered within the particle interior, ruling out mechanisms that rely on surface accessibility. Second, DFT modeling reveals no energetic stabilization of NO_3^- near T_d sites, falsifying the proposed defect–impurity coupling pathway. Third, comparative NMR analysis shows that T_d defects are also present in chloride-bearing gibbsite, which exhibits high radiolytic H_2 yields, eliminating T_d as a structural marker for radiolytic suppression. These constraints converge on a shared conclusion that T_d is a reproducible, subsurface feature of synthetic gibbsite, but it plays no mechanistic role in nitrate-linked radiolytic stability. The residual explanation for radiolytic stability is therefore chemical, not structural. Given the known redox reactivity of NO_3^-, its function as an electron scavenger now emerges as the leading candidate mechanism for suppressing radiolytic hydrogen production in these materials.

Conclusions

This study exemplifies a constraint-based approach to mechanistic materials characterization, using orthogonal experimental and computational methods to eliminate structurally plausible but ultimately incorrect explanations. By clarifying what does not govern radiolytic suppression in gibbsite, this work narrows the mechanistic search space and strengthens the case for chemically driven electron-scavenging processes. The structural resolution provided here, combined with the elimination of defect-based models, offers a refined foundation for future efforts to resolve and exploit redox-mediated radiation resistance in aluminum hydroxides.

Experimental and computational methods

Synthesis

Euhedral, hexagonal gibbsite nanoplates were synthesized by mild hydrothermal treatment of an amorphous aluminum hydroxide precursor precipitated from the neutralization of aqueous aluminum nitrate.[20] A solution of 0.25 M aluminum nitrate nonahydrate in water was prepared and titrated, using 1.0 M sodium hydroxide until a pH of 5 was attained. The precipitated gel dispersion was mixed for 1 h, collected by centrifugation and redispersed in water 3 times to remove Na^+ and NO_3^- ions. After decanting the third wash, the pelleted gel was dispersed in water (0.3 g pelleted gel per mL of water) and transferred to a 22 mL Teflon lined Parr vessel. The Parr vessel

was heated in a rotary oven for 72 h at 80 °C and 10 rpm. The product was collected and washed by centrifugation, redispersed in water 3 times, and finally dried in an oven at 80 °C overnight. Whereas NO_3-gibbsite was synthesized with aluminum nitrate nonahydrate as the precursor, syntheses of Cl-gibbsite substituted aluminum chloride and then used identical procedures. Note that the amorphous precursor phase has been described previously[16] and exhibits no significant Bragg diffraction. Following hydrothermal treatment, XRD patterns and NMR spectroscopy confirmed the formation of gibbsite.[16]

Synthesis of Cr-adsorbed gibbsite

Detailed in depth elsewhere,[12] different concentrations of Cr were used for the adsorption experiments. Solutions of 100 and 5 ppm Cr were prepared by dissolving chromium(III) nitrate nonahydrate. Then dispersions comprised of 200 mg of NO_3-gibbsite in 200 mL of solution in a 250 mL centrifuge tube were prepared. To fully disperse the solutions, the solutions were sonicated for 30 minutes and then shaken in an orbital shaker for about 16 h. After shaking, the gibbsite adsorption solids were isolated from the solution through centrifugation at 8600 rpm for 30 minutes. The solid precipitate resulting from the centrifugation was isolated, washed once with DI water, and were dried in a 50 °C oven.

Scanning electron microscopy

A Helios NanoLab 600i SEM (FEI, Hillsoboro, OR) was used. Before imaging, the sample was sputter coated with approximately 5 nm of carbon. The image was processed in imageJ, where the contrast was optimized, and a scale bar was added.

14.1 T NMR spectroscopy

Solid-state NMR spectra were acquired on a Bruker spectrometer operating at a field strength of 14.0954 T, corresponding to a ^{27}Al Larmor frequency of 156.375 MHz, using a 2.5 mm MAS probe. Spectra were acquired at 25 °C using a single-pulse, direct-excitation sequence with a calibrated $\pi/20$ pulse of 0.450 μs duration. Approximately 80 000 transients were collected with a recycle delay of 0.5 s and an acquisition time of 9.8 ms. A magic-angle spinning (MAS) rate of 20 kHz was used for the data presented. Chemical shifts were externally referenced to a 1.0 M aqueous $Al(H_2O)_6^{3+}$ solution at 0 ppm. Post-acquisition processing of the ^{27}Al MAS NMR spectra was performed in MestReNova (v. 14.01). The free induction decay was zero-filled to 26 ms, and an exponential line broadening of 20 Hz was applied.

18.8 Dynamic nuclear polarization NMR

Samples of NO_3-gibbsite and α-alumina were prepared for DNP NMR analysis by incipient wetness impregnation. The solid powder was wetted with a sufficient volume of a cryogenic matrix solution composed of [d_8-glycerol/D_2O/H_2O (60/30/10 v/v/v)] containing 36 mM of the biradical polarizing agent TinyPol. The resulting damp powder was packed into a 1.9 mm ZrO_2 MAS rotor and sealed with a Vespel drive cap.

All DNP-enhanced solid-state NMR experiments were performed on a Bruker Avance NEO 800 MHz (18.8 T) spectrometer equipped with a 1.9 mm H/X/Y low-temperature DNP/MAS probe, operating at ^{1}H and ^{27}Al Larmor frequencies of 800.1 MHz and 208.50 MHz, respectively. Dynamic nuclear polarization was achieved by continuous microwave irradiation from a Bruker gyrotron operating at 526.932 GHz, with a power of approximately 8 W for gibbsite and 13 W for α-alumina. For all DNP experiments, the sample temperature was maintained at 100 K, and the magic-angle spinning (MAS) rate was 15 kHz.

For both materials, ^{27}Al {^{1}H} cross-polarization (CP) MAS spectra were acquired with a ^{1}H 90° pulse of 3.0 μs, a recycle delay of 30.0 s, and high-power SPINAL-64 ^{1}H decoupling during acquisition. For gibbsite, the CP contact time was 2.0 ms, and 64 scans were averaged for both DNP-on and DNP-off experiments. For α-alumina, the contact time was 1.8 ms (DNP-on, 320 scans) and 1.6 ms (DNP-off, 64 scans). Additionally, a quantitative ^{27}Al direct polarization (DP) MAS spectrum of α-alumina was acquired using a small tip-angle pulse (0.75 μs) with a 2.0 s recycle delay, averaging 32 scans. The DNP signal enhancement factor (ε) was calculated from the ratio of integrated intensities of the DNP-on (Ion) and DNP-off (Ioff) spectra, normalizing for the number of scans (NS) where appropriate with the equation, ε = (Ion/NSon)/(Ioff/NSoff). This resulted in ε = 18 for the gibbsite sample and ε = 24 for the α-alumina. Given the slight change in contact time for α-alumina, the associated ε is approximate.

All NMR data were processed using MestReNova (v.16.0.0-392765). Acquired FIDs (8192 complex points) were processed with an exponential line broadening of 20 Hz and were zero-filled to 16 384 points prior to Fourier transformation. The ^{27}Al chemical shift scale was referenced to the apparent peak maximum of the prominent gibbsite signal in the CP MAS NMR spectrum, which was assigned a chemical shift of 10 ppm, which is an approximation of the isotropic chemical shift of the 2 Al sites in gibbsite (13.6 and 11.3 ppm, respectively).[15]

DFT simulations

Density functional theory (DFT) calculations were performed to investigate a plausible formation mechanism for the subsurface T_d defects observed experimentally. All calculations were conducted using the Vienna *Ab initio* Simulation Package (VASP).[21] Electron-ion interactions were described using standard projector augmented-wave (PAW)[22] pseudopotentials with 5, 6, 3 and 1 explicit electrons for N, O, Al, and H, respectively. Spin unpolarized structural relaxations were completed within the RPBE-D3 exchange-correlation approximation,[23,24] Initial models were obtained by removing $[Al(OH)_n]^{3-n}$, n = 3,4 from a 2 × 2 × 1 supercell of gibbsite and introducing a relaxed gas phase $[Al(OH)_3NO_3]^-$ group (Fig. 5A). A 2 × 3 × 3 Gamma-centered *k*-point grid was used. Internal coordinates and the cell vectors were relaxed until all forces were less than 0.01 eV Å^{-1} in two steps: with an energy cutoff of (i) 300 eV and (ii) 600 eV. The NO_3^- was charged balanced by a uniform positive background for n = 4. Dipole corrections were not applied because the modeled defects are neutral, the periodic bulk medium

screens defect–defect interactions, and the supercells are non-cubic, where correction terms are not valid. The final, relaxed structure was visualized using VESTA. The coordination environments of the Al atoms were analyzed to identify changes induced by the interstitial NO_3^-. The optimized CONTCAR files and representative structural visualizations are provided in the SI.

Conflicts of interest

There are no conflicts to declare.

Data availability

Data available upon reasonable request.

Supplementary information (SI) is available. See DOI: https://doi.org/10.1039/d5qi01703c.

Acknowledgements

This research was primarily supported by IDREAM (Ion Dynamics in Radioactive Environments and Materials), an Energy Frontier Research Center funded by the U.S. Department of Energy (DOE), Office of Science, Basic Energy Science (FWP 68932). Mateusz Dembowski is thanked for acquiring the micrograph of NO_3-gibbsite. A large language model assisted with language editing. DNP-NMR spectroscopy experiments were supported by the Physical and Computational Sciences Directorate, Laboratory Directed Research and Development (LDRD) Program at Pacific Northwest National Laboratory (PNNL) and were performed using facilities at the Environmental Molecular Science Laboratory (grid.436923.9), a DOE Office of Science User Facility sponsored by the Office of Biological and Environmental Research at PNNL. PNNL is a multi-program national laboratory operated for the DOE by Battelle Memorial Institute under Contract No. DE-AC05-76RL01830.

References

1 J. A. Kaddissy, *et al.*, Radiolytic Events in Nanostructured Aluminum Hydroxides, *J. Phys. Chem. C*, 2017, **121**, 6365–6373, DOI: 10.1021/acs.jpcc.6b13104.

2 A. Westesen and R. Peterson, Speciation of aluminum phases at the Hanford Site, *Environ. Prog. Sustainable Energy*, 2022, **41**, e13789, DOI: 10.1002/ep.13789.

3 R. A. Peterson, *et al.*, Review of the Scientific Understanding of Radioactive Waste at the U.S. DOE Hanford Site, *Environ. Sci. Technol.*, 2018, **52**, 381–396, DOI: 10.1021/acs.est.7b04077.

4 H. Hlushko, *et al.*, Effect of impurities on radical formation in gibbsite radiolysis, *Phys. Chem. Chem. Phys.*, 2024, **26**, 9867–9870, DOI: 10.1039/D3CP06305D.

5 E. Briley, P. Huestis, X. Zhang, K. M. Rosso and J. A. LaVerne, Radiolysis of thermally dehydrated gibbsite, *Mater. Chem. Phys.*, 2021, **271**, 124885, DOI: 10.1016/j.matchemphys.2021.124885.

6 S. Wang, *et al.*, Two-step route to size and shape controlled gibbsite nanoplates and the crystal growth mechanism, *CrystEngComm*, 2020, **22**, 2555–2565, DOI: 10.1039/D0CE00114G.

7 S. T. Mergelsberg, *et al.*, Cluster defects in gibbsite nanoplates grown at acidic to neutral pH, *Nanoscale*, 2021, **13**, 17373–17385, DOI: 10.1039/D1NR01615F.

8 J. Koppe and A. J. Pell, Structure Determination and Refinement of Paramagnetic Materials by Solid-State NMR, *ACS Phys. Chem. Au*, 2023, **3**, 419–433, DOI: 10.1021/acsphyschemau.3c00019.

9 J. Kim, *et al.*, 2H and 27Al Solid-State NMR Study of the Local Environments in Al-Doped 2-Line Ferrihydrite, Goethite, and Lepidocrocite, *Chem. Mater.*, 2015, **27**, 3966–3978, DOI: 10.1021/acs.chemmater.5b00856.

10 R. Kellner, *et al.*, SEMPRE: Spectral Editing Mediated by Paramagnetic Relaxation Enhancement, *J. Am. Chem. Soc.*, 2009, **131**, 18016–18017, DOI: 10.1021/ja905412z.

11 Q. Miao, *et al.*, Paramagnetic Chemical Probes for Studying Biological Macromolecules, *Chem. Rev.*, 2022, **122**, 9571–9642, DOI: 10.1021/acs.chemrev.1c00708.

12 Y. Zhao, *et al.*, Understanding Trace Iron and Chromium Incorporation During Gibbsite Crystallization and Effects on Mineral Dissolution, *Environ. Sci. Technol.*, 2024, **58**, 20125–20136, DOI: 10.1021/acs.est.4c04483.

13 A. J. Rossini, *et al.*, Dynamic Nuclear Polarization Surface Enhanced NMR Spectroscopy, *Acc. Chem. Res.*, 2013, **46**, 1942–1951, DOI: 10.1021/ar300322x.

14 A. Lesage, *et al.*, Surface Enhanced NMR Spectroscopy by Dynamic Nuclear Polarization, *J. Am. Chem. Soc.*, 2010, **132**, 15459–15461, DOI: 10.1021/ja104771z.

15 C. V. Chandran, *et al.*, Alumina: discriminative analysis using 3D correlation of solid-state NMR parameters, *Chem. Soc. Rev.*, 2019, **48**, 134–156, DOI: 10.1039/C8CS00321A.

16 J. Z. Hu, *et al.*, Transitions in Al Coordination during Gibbsite Crystallization Using High-Field 27Al and 23Na MAS NMR Spectroscopy, *J. Phys. Chem. C*, 2017, **121**, 27555–27562, DOI: 10.1021/acs.jpcc.7b10424.

17 D. A. Ksenofontov and Y. K. Kabalov, Structure refinement and thermal stability of gibbsite, *Inorg. Mater.*, 2012, **48**, 142–144, DOI: 10.1134/S0020168512020136.

18 K. Momma and F. Izumi, VESTA 3 for three-dimensional visualization of crystal, volumetric and morphology data, *J. Appl. Crystallogr.*, 2011, **44**, 1272–1276, DOI: 10.1107/S0021889811038970.

19 A. R. Brough, C. P. Grey and C. M. Dobson, Paramagnetic ions as structural probes in solid-state NMR: distance measurements in crystalline lanthanide acetates, *J. Am. Chem. Soc.*, 1993, **115**, 7318–7327, DOI: 10.1021/ja00069a034.

20 X. Zhang, *et al.*, Fast Synthesis of Gibbsite Nanoplates and Process Optimization using Box-Behnken Experimental

Design, *Cryst. Growth Des.*, 2017, **17**, 6801–6808, DOI: **10.1021/acs.cgd.7b01400**.

21 G. Kresse and J. Furthmüller, Efficient iterative schemes for ab initio total-energy calculations using a plane-wave basis set, *Phys. Rev. B: Condens. Matter Mater. Phys.*, 1996, **54**, 11169–11186, DOI: **10.1103/PhysRevB.54.11169**.

22 P. E. Blöchl, Projector augmented-wave method, *Phys. Rev. B: Condens. Matter Mater. Phys.*, 1994, **50**, 17953–17979, DOI: **10.1103/PhysRevB.50.17953**.

23 B. Hammer, L. B. Hansen and J. K. Nørskov, Improved adsorption energetics within density-functional theory using revised Perdew-Burke-Ernzerhof functionals, *Phys. Rev. B:Condens. Matter Mater. Phys.*, 1999, **59**, 7413–7421, DOI: **10.1103/PhysRevB.59.7413**.

24 S. Grimme, J. Antony, S. Ehrlich and H. Krieg, A consistent and accurate ab initio parametrization of density functional dispersion correction (DFT-D) for the 94 elements H-Pu, *J. Chem. Phys.*, 2010, **132**, 154104, DOI: **10.1063/1.3382344**.